Commun. Comput. Phys.
doi: 10.4208/cicp.OA-2024-0242

Vol. **39**, No. 5, pp. 1559-1588
May 2026

Adaptive Reconstruction Method Using Discontinuity Feedback for High-Order Accuracy Schemes

Hong Zhang[1], Yue Zhao[2], Xing Ji[1,*] and Kun Xu[3,4,5]

[1] *State Key Laboratory for Strength and Vibration of Mechanical Structures, School of Aerospace Engineering, Xi'an Jiaotong University, Xi'an 710000, P.R. China.*
[2] *China Academy of Launch Vehicle Technology, Beijing, China.*
[3] *Department of Mathematics, Hong Kong University of Science and Technology, Clear Water Bay, Kowloon 999077, Hong Kong SAR.*
[4] *Department of Mechanical and Aerospace Engineering, Hong Kong University of Science and Technology, Clear Water Bay, Kowloon 999077, Hong Kong SAR.*
[5] *Shenzhen Research Institute, Hong Kong University of Science and Technology, Shenzhen 518000, China.*

Received 7 October 2024; Accepted (in revised version) 24 January 2025

Abstract. This paper presents efficient adaptive stencil extension reconstruction methods using a discontinuity feedback factor to address weak robustness and high computational costs in high-order schemes (7th-order and above). The method features two innovations: accuracy order adaptively increases from the lowest level based on local stencil smoothness, unlike WENO and MUSCL limiters that reduce order from highest level; and the Discontinuity Feedback Factor detects sub-cell discontinuity strength while serving as a local smoothness measure. This eliminates expensive smoothness indicators in very high-order schemes and generalizes to arbitrary high orders. Rigorous tests, including a Mach 20000 jet, demonstrate exceptional robustness.

AMS subject classifications: 52B10, 65D18, 68U05, 68U07

Key words: Computational efficiency, discontinuity feedback factor, adaptive stencil extension, high-order schemes.

1 Introduction

Contemporary CFD research emphasizes developing high-order schemes for turbulent flow simulation, building on Harten et al.'s foundational work [12]. Key methodological advances include Essential Non-Oscillatory (ENO) schemes [12,30], Weighted Essential

---

*Corresponding author. *Email addresses:* `zhanghong2001@stu.xjtu.edu.cn` (H. Zhang), `kgfit@163.com` (Y. Zhao), `jixing@xjtu.edu.cn` (X. Ji), `makxu@ust.hk` (K. Xu)

Non-Oscillatory (WENO) schemes [19,26], and Discontinuous Galerkin (DG) methods [6, 7], which have enhanced capabilities for handling complex flow problems with improved accuracy and efficiency.

High-order numerical methods face two significant challenges. First, algorithm robustness decreases rapidly with increasing order when calculating discontinuity problems. Recent improvements include new stencil selection strategies, combining nonlinear and linear weights [10, 27], and TENO schemes that adapt to local flow characteristics [19,30]. Limiters provide another approach, though prior limiters (van Leer [32], van Albada [32]) are parameter-sensitive and post limiters like MOOD [5] are computationally intensive. Second, these schemes are computationally expensive. While one-stage high-order methods [24] reduce temporal advancement costs compared to classical Runge-Kutta approaches, spatial reconstruction remains challenging. WENO schemes require complex smoothness indicators, especially at higher orders. Current solutions include using lower-order stencil combinations [14, 20, 21] and weighted-least-squares methods [13, 25], but these either lack arbitrary high-order applicability or suffer from weak robustness and non-unified global smoothness indicators.

In order to deal with the above challenges, the Adaptive Stencil Extension reconstruction methods based on Discontinuity Feedback factor (ASE-DF) are constructed. As presented in Section 3.1, DF is to define the discontinuity strength associated with the stencil-based reconstruction. Without imposing the continuous flow distribution assumption inside each cell, the use of DF makes it more flexible in developing high-order FVM and its transition to be first-order scheme for preserving positivity property. The use of DF not only improves the robustness of the algorithm, but also replaces the smoothness indicators for each stencil, which significantly reduces the computational cost while achieving arbitrary high-order schemes. In the DF-based schemes presented in this paper, two flux functions are considered. The first one is the Lax-Friedrichs (L-F) with the SSP-RK [11] temporal discretization, which has the positivity stability preserving, and the other is the 2nd-order gas-kinetic scheme (GKS) [34,35] with two-stages fourth-order (S2O4) temporal discretization.

This paper is organized as follows: Section 2 provides a brief overview of the high-order finite volume scheme. Section 3 introduces the ASP-DF reconstruction methods. In Section 4, some numerical results of the viscous and inviscid flow problems will be presented. The last section is the conclusion.

2 High-order finite volume scheme

2.1 Finite volume framework

The Finite Volume Method (FVM) involves dividing the computational domain into a finite amount of control volumes. Within each control volume, the physical quantities are integrated and averaged, resulting in the discrete equations

$$\int_{\Omega_{ij}} \mathbf{W}(\mathbf{x},t^{n+1})\mathrm{d}V = \int_{\Omega_{ij}} \mathbf{W}(\mathbf{x},t^{n})\mathrm{d}V - \int_{t^n}^{t^{n+1}} \int_{\partial\Omega_{ij}} \mathbf{F}\cdot\mathbf{n}\mathrm{d}S, \tag{2.1}$$

where $\mathbf{W}=(\rho,\rho U,\rho V,\rho E)^T$ are the conservative variables in a control volume $\mathbf{\Omega}_{ij}$, and $\mathbf{F}$ are the fluxes across the $\partial\mathbf{\Omega}_{ij}$. $\partial\mathbf{\Omega}_{ij}$ corresponds to the cell interfaces, and in a 2-D rectangular mesh, the boundary $\partial\mathbf{\Omega}_{ij}$ can be expressed as

$$\partial\mathbf{\Omega}_{ij} = \bigcup_{m=1}^{4} \mathbf{\Gamma}_{ij,m}, \tag{2.2}$$

where $\mathbf{\Gamma}_{ij,p}$ denotes the pth interface of the $\mathbf{\Omega}_{ij}$. Integrating over the cell $\mathbf{\Omega}_{ij}$, the semi-discrete form of Eq. (2.1) can be obtained as follows [17]

$$\frac{\mathrm{d}\mathbf{W}_{ij}}{\mathrm{d}t} = \mathcal{L}(\mathbf{W}_{ij}) = -\frac{1}{|\mathbf{\Omega}_{ij}|}\sum_{m=1}^{4}\oint_{\mathbf{\Gamma}_{ij,m}} \mathbf{F}(\mathbf{W}_{ij})\cdot\mathbf{n}_m\mathrm{d}s, \tag{2.3}$$

where $\mathbf{W}_{ij}$ is the cell average variables over the $\mathbf{\Omega}_{ij}$, $|\mathbf{\Omega}_{ij}|$ is the area of $\mathbf{\Omega}_{ij}$. $\mathcal{L}(\mathbf{W})$ is the temporal derivatives of the conservative variables, $\mathbf{F}=(F,G)^T$ are the flux function, and $\mathbf{n}_m$ corresponds to the outer normal direction of the interface $\mathbf{\Gamma}_{ij,m}$.

To achieve the high-order scheme, Gaussian points are considered. The line integral over $\mathbf{\Gamma}_{ij,m}$ is discretized according to Gaussian quadrature as follows

$$\oint_{\mathbf{\Gamma}_{ij,m}} \mathbf{F}(\mathbf{W}_{ij})\cdot\mathbf{n}_m\mathrm{d}s = |l_m|\sum_{k=1}^{p}\eta_k\mathbf{F}(\mathbf{x}_{m,k},t)\cdot\mathbf{n}_m, \tag{2.4}$$

where $\mathbf{x}_{m,k}$ for $\mathbf{\Gamma}_{ij,m}$ are the Gaussian points, η_k is the weight of the kth Gaussian point, and $|l_m|$ corresponds to the length of the $\Gamma_{ij,m}$. Theoretically, $\frac{r+1}{2}$ Gaussian points should be used for rth order accuracy, while $\frac{r-1}{2}$ Gaussian points combined with S2O4 method can achieve the theoretical accuracy and improving computational efficiency. Therefore, for rth order spatial accuracy, $\frac{r-1}{2}$ Gaussian points are used in this paper.

To update the flow variables in global coordinates, first we need to obtain the conservative variables in the local coordinate

$$\widetilde{\mathbf{W}} = \mathbf{T}\mathbf{W},$$

where the rotation matrix $\mathbf{T}$ for the 2-D case has the form

$$\mathbf{T} = \begin{pmatrix} 1 & 0 & 0 & 0 \\ 0 & \cos\theta & \sin\theta & 0 \\ 0 & -\sin\theta & \cos\theta & 0 \\ 0 & 0 & 0 & 1 \end{pmatrix}.$$

Then we can obtain the fluxes in the local coordinate

$$\widetilde{\mathbf{F}}(\mathbf{x}_{m,k},t)=\int \boldsymbol{\psi}\widetilde{u}f(\widetilde{\mathbf{x}}_{m,k},t,\widetilde{\mathbf{u}},\xi)\mathrm{d}\widetilde{\mathbf{u}}\mathrm{d}\xi. \tag{2.5}$$

According to [28], the global and local fluxes are related as

$$\mathbf{F}(\mathbf{x}_{m,k},t)\cdot\mathbf{n}=\mathbf{T}^{-1}\widetilde{\mathbf{F}}(\widetilde{\mathbf{x}}_{m,k},t),$$

here $\mathbf{F}$ and $\widetilde{\mathbf{F}}$ are the gas-kinetic fluxes, which will be presented in Section 2.2.

2.2 Gas-kinetic flux solver and two-stage fourth-order temporal discretization

The BGK equation [2] can be written as

$$f_t+\mathbf{u}\cdot\nabla f=\frac{g-f}{\tau}, \tag{2.6}$$

where f is the gas distribution function, g is the corresponding equilibrium state, and τ is the collision time. The collision term satisfied the compatibility condition

$$\int \frac{g-f}{\tau}\boldsymbol{\psi}\mathrm{d}\Xi=0, \tag{2.7}$$

where $\boldsymbol{\psi}=\left(1,u,v,\frac{1}{2}(u^2+v^2+\xi^2)\right)^T$, $\mathrm{d}\Xi=\mathrm{d}u\mathrm{d}v\mathrm{d}\xi_1\cdots\mathrm{d}\xi_K$, (u,v) are the two components of the macroscopic particle velocities, $\xi=(\xi_1,\cdots,\xi_K)$ correspond to the components of the internal particle velocities in K dimensions, and K is the number of the internal freedom. $K=(4-2\gamma)/(\gamma-1)$ for 2-D flows, and γ is the specific heat ratio.

The general macroscopic gas dynamic equations can be obtained through the Chapman-Enskog expansion [4] of the BGK equation, and the gas distribution function can be expressed as

$$f=g-\tau D_{\mathbf{u}}g+\tau D_{\mathbf{u}}(\tau D_{\mathbf{u}})g-\tau D_{\mathbf{u}}[\tau D_{\mathbf{u}}(\tau D_{\mathbf{u}})g]+\cdots, \tag{2.8}$$

where $D_{\mathbf{u}}=\partial/\partial t+\mathbf{u}\cdot\nabla$. When $f=g$, the equation takes the form of Euler equation, and the Navier-Stokes equation can be obtained by the truncated 1st-order distribution function

$$f=g-\tau(ug_x+vg_y+g_t).$$

The integral solution of Eq. (2.6) is

$$f(\mathbf{x}_{m,k},t,\mathbf{u},\xi)=\frac{1}{\tau}\int_0^t g(\mathbf{x}',t',\mathbf{u},\xi)e^{-(t-t')/\tau}dt'+e^{-t/\tau}f_0(\mathbf{x}_{m,k},-\mathbf{u}t,\mathbf{u},\xi), \tag{2.9}$$

where $\mathbf{x}_{m,k}=(0,0)$ is the quadrature point at the interface in the local coordinates, and $\mathbf{x}_{m,k}=\mathbf{x}'+\mathbf{u}(t-t')$ is the trajectory of the particles, f_0 corresponds to the initial gas distribution function, and g is the corresponding equilibrium state. Then we can construct a 2nd-order time accuracy gas distribution function [35] at the local Gaussian point $\mathbf{x}_{m,k}=(0,0)$

$$
\begin{aligned}
f(\mathbf{x}_{m,k},t,\mathbf{u},\xi)=&\left(1-e^{-t/\tau_n}\right)g^c\\
&+\left[(t+\tau)e^{-t/\tau_n}-\tau\right]a^c_{\mathbf{x}}\cdot\mathbf{u}g^c+\left(t-\tau+\tau e^{-t/\tau_n}\right)A^cg^c\\
&+e^{-t/\tau_n}g^l\left[1-(\tau+t)a^l_{\mathbf{x}}\cdot\mathbf{u}-\tau A^l\right]\mathbb{H}(u)\\
&+e^{-t/\tau_n}g^r[1-(\tau+t)a^r_{\mathbf{x}}\cdot\mathbf{u}-\tau A^r][1-\mathbb{H}(u)],
\end{aligned}
\tag{2.10}
$$

where $\mathbb{H}$ is the Heaviside function. The functions $g^{l,r,c}$ correspond to the initial gas distribution function on the left and right sides of the cell interface, and the equilibrium state located at the interface, respectively. The flow dynamics at the interface are contingent upon the ratio of the time step to the local particle collision time.

The function $g^k,k=l,r$ satisfies Maxwell's distribution

$$
g^k=\rho^k\left(\frac{\lambda^k}{\pi}\right)^{\frac{K+3}{2}}e^{-\lambda^k\left[(u-U^k)^2+(v-V^k)^2+\xi^2\right]},
\tag{2.11}
$$

where λ is a function of temperature, molecular mass and the Boltzmann constant. g^k can be determined by

$$
\int\boldsymbol{\psi}g^l\mathrm{d}\Xi=\mathbf{W}^l,\quad\int\boldsymbol{\psi}g^r\mathrm{d}\Xi=\mathbf{W}^r,
\tag{2.12}
$$

where $\mathbf{W}^l,\mathbf{W}^r$ are the reconstructed variables, which will be presented in Section 3.

The coefficients $a_{\mathbf{x}}$, A denote the spatial and temporal derivatives, respectively, which have the form

$$
a_{\mathbf{x}}\equiv(\partial g/\partial\mathbf{x})/g=g_{\mathbf{x}}/g,\quad A\equiv(\partial g/\partial t)/g=g_t/g,
$$

which can be determined by the spatial derivatives of $\mathbf{W}$ and the compatibility condition as follows

$$
\begin{aligned}
&\langle a_x\rangle=\frac{\partial\mathbf{W}}{\partial x}=\mathbf{W}_x,\quad\langle a_y\rangle=\frac{\partial\mathbf{W}}{\partial y}=\mathbf{W}_y,\\
&\langle A+a_xu+a_yv\rangle=0,
\end{aligned}
$$

where $a_x=(a_{x1},a_{x2}u,a_{x3}v,a_{x4}\frac{1}{2}(u^2+v^2+\xi^2))^T$ and a_y has the similar form. $\langle\cdots\rangle$ are the moments of a gas distribution function defined by

$$
\rho\langle(\cdots)\rangle=\int(\cdots)g\mathrm{d}\Xi.
\tag{2.13}
$$

More details about the integration calculation can be found in Appendix A. Similarly, the equilibrium state g^c and its derivatives $a^c_{\mathbf{x}}$ can be obtained by the reconstructed values $\mathbf{W}^c,\mathbf{W}^c_{\mathbf{x}}$, which will be presented in Section 3.5.

The physical collision time τ in the exponential function can be modified with a numerical collision time τ_n to capture unresolved discontinuities. For inviscid flow, the numerical collision time τ_n takes the following form [35]

$$\tau_n = C_1\Delta t + C_2\left|\frac{p^l-p^r}{p^l+p^r}\right|\Delta t, \tag{2.14}$$

where C_1,C_2 are constants, p^l,p^r denote the pressure on the left and right side of the cell interface, respectively. For the viscous flow, τ_n is enlarged according to the normalized pressure difference [35]

$$\tau_n = \tau + C_2\left|\frac{p^l-p^r}{p^l+p^r}\right|\Delta t = \frac{\mu}{p} + C_2\left|\frac{p^l-p^r}{p^l+p^r}\right|\Delta t, \tag{2.15}$$

where μ is the dynamical viscosity coefficient. The reason for incorporating the pressure jump term to enlarge the particle collision time is to maintain the non-equilibrium dynamics within the shock layer via kinetic particle transport.

The two-stage fourth-order (S2O4) temporal discretization was developed in CFD applications [23,29], which has the form

$$\begin{aligned}
&\mathbf{W}_{ij}^{*} = \mathbf{W}_{ij}^{n} + \frac{1}{2}\Delta t\mathcal{L}(\mathbf{W}_{ij}^{n}) + \frac{1}{8}\Delta t^2\frac{\partial}{\partial t}\mathcal{L}(\mathbf{W}_{ij}^{n}),\\
&\mathbf{W}_{ij}^{n+1} = \mathbf{W}_{ij}^{n} + \Delta t\mathcal{L}(\mathbf{W}_{ij}^{n}) + \frac{1}{6}\Delta t^2\left(\frac{\partial}{\partial t}\mathcal{L}(\mathbf{W}_{ij}^{n}) + 2\frac{\partial}{\partial t}\mathcal{L}(\mathbf{W}_{ij}^{*})\right),
\end{aligned} \tag{2.16}$$

where $\frac{\partial}{\partial t}\mathcal{L}(\mathbf{W})$ are the time derivatives of the flux transport integrated over the closed interfaces of the cell.

It is needed to obtain the first-order time derivatives of the flux at t_n and $t^* = t_n + \Delta t/2$ through the GKS flux function. The total flux transport at the Gaussian point $x_{m,k}$ over the time interval δ is expressed as

$$\mathbb{F}^n(\mathbf{x}_{m,k},\delta) = \int_{t_n}^{t_n+\delta}\mathbf{F}^n(\mathbf{x}_{m,k},t)\mathrm{d}t = \int_{t_n}^{t_n+\delta}\int u\boldsymbol{\psi} f(\mathbf{x}_{m,k},t,\mathbf{u},\xi)\mathrm{d}\Xi\mathrm{d}t. \tag{2.17}$$

For the 2nd-order GKS solver, let $t_n = 0$, the flux can be approximated as a linear function

$$\mathbf{F}^n(\mathbf{x}_{m,k},t) = \mathbf{F}^n(\mathbf{x}_{m,k}) + \partial_t\mathbf{F}^n(\mathbf{x}_{m,k})t. \tag{2.18}$$

Substituting Eq. (2.18) into Eq. (2.17), we can obtained

$$\begin{aligned}
&\mathbf{F}^n(\mathbf{x}_{m,k})\Delta t + \frac{1}{2}\partial_t\mathbf{F}^n(\mathbf{x}_{m,k})\Delta t^2 = \mathbb{F}^n(\mathbf{x}_{m,k},\Delta t),\\
&\frac{1}{2}\partial_t\mathbf{F}^n(\mathbf{x}_{m,k})\Delta t + \frac{1}{8}\partial_t\mathbf{F}^n(\mathbf{x}_{m,k})\Delta t^2 = \mathbb{F}^n(\mathbf{x}_{m,k},\Delta t/2).
\end{aligned} \tag{2.19}$$

Eq. (2.19) is a linear system, and its solution is

$$\begin{aligned}&\mathbf{F}^n(\mathbf{x}_{m,k})=(4\mathbb{F}^n(\mathbf{x}_{m,k},\Delta t/2)-\mathbb{F}^n(\mathbf{x}_{m,k},\Delta t))/\Delta t,\\&\partial_t\mathbf{F}^n(\mathbf{x}_{m,k})=4(\mathbb{F}^n(\mathbf{x}_{m,k},\Delta t)-2\mathbb{F}^n(\mathbf{x}_{m,k},\Delta t/2))/\Delta t^2.\end{aligned}$$

Finally, the $\mathcal{L}(\mathbf{W}_{ij}^n)$ and its time derivatives $\frac{\partial}{\partial t}\mathcal{L}(\mathbf{W}_{ij}^n)$ can be obtained by

$$\begin{aligned}&\mathcal{L}(\mathbf{W}_{ij}^n)=-\frac{1}{\Omega_{ij}}\sum_{m=1}^{4}|l_m|\sum_{k=1}^{p}\eta_k\mathbf{F}^n(\mathbf{x}_{m,k})\cdot\mathbf{n}_m,\\&\frac{\partial}{\partial t}\mathcal{L}(\mathbf{W}_{ij}^n)=-\frac{1}{\Omega_{ij}}\sum_{m=1}^{4}|l_m|\sum_{k=1}^{p}\eta_k\partial_t\mathbf{F}^n(\mathbf{x}_{m,k})\cdot\mathbf{n}_m.\end{aligned}\tag{2.20}$$

In this way, all variables needed in Eq (2.16) are determined.

2.3 Lax-Friedrichs flux solver and RK temporal discretization

To evaluate the robustness of the new reconstruction methods, the widely used Riemann solver, i.e., Lax-Freidrichs (L-F) flux is also considered. The 2-D Euler equations can be expressed as

$$\begin{pmatrix}\rho\\\rho U\\\rho V\\\rho E\end{pmatrix}_t+\begin{pmatrix}\rho U\\\rho U^2+p\\\rho UV\\U(\rho E+p)\end{pmatrix}_x+\begin{pmatrix}\rho V\\\rho UV\\\rho V^2+p\\V(\rho E+p)\end{pmatrix}_y=0.\tag{2.21}$$

The L-F method [31] is a numerical method for the solution of hyperbolic partial differential equations. The 1st-order L-F flux function can be expressed as

$$\begin{aligned}\mathbf{F}(\mathbf{W}_{i+1/2})=&\frac{1}{2}(\mathbf{F}(\mathbf{W}_{i+1/2}^l)+\mathbf{F}(\mathbf{W}_{i+1/2}^r))\\&-\frac{1}{2}\max\{|U_{i+1/2}^l|+c_{i+1/2}^l,|U_{i+1/2}^r|+c_{i+1/2}^r\}(\mathbf{W}_{i+1/2}^r-\mathbf{W}_{i+1/2}^l),\end{aligned}\tag{2.22}$$

where $\mathbf{F}(\mathbf{W}^{l,r})=\left(\rho^{l,r}U^{l,r},\rho^{l,r}U^{l,r}U^{l,r}+p^{l,r},\rho^{l,r}U^{l,r}V^{l,r},U^{l,r}(\rho^{l,r}E^{l,r}+p^{l,r})\right)^T$ correspond to the flux on the left and right side of the interface, and $c^{l,r}=\sqrt{\frac{\gamma p^{l,r}}{\rho^{l,r}}}$ is the speed of sound.

The 3rd-order strong stability preserving Runge-Kutta (SSP-RK3) [11] temporal discretization has been developed because of its strong robust, which has the form

$$\begin{aligned}&\mathbf{W}_{ij}^{(1)}=\mathbf{W}_{ij}^n+\Delta t\mathcal{L}(\mathbf{W}_{ij}^n),\\&\mathbf{W}_{ij}^{(2)}=\frac{3}{4}\mathbf{W}_{ij}^n+\frac{1}{4}\mathbf{W}_{ij}^{(1)}+\frac{1}{4}\Delta t\mathcal{L}(\mathbf{W}_{ij}^{(1)}),\\&\mathbf{W}_{ij}^{n+1}=\frac{1}{3}\mathbf{W}_{ij}^n+\frac{2}{3}\mathbf{W}_{ij}^{(2)}+\frac{2}{3}\Delta t\mathcal{L}(\mathbf{W}_{ij}^{(2)}).\end{aligned}\tag{2.23}$$

3 Adaptive stencil extension with discontinuous feedback reconstruction in zero-mean form

In this section, an efficient class of high-order Adaptive Stencil Extension reconstructions with Discontinuous Feedback factor (ASE-DF) are presented. Compared to the classical WENO schemes, the ASE-DF schemes can improve computational efficiency, and significantly enhance the robustness of the algorithm.

In this section, to reconstruct the left interface value $\mathbf{W}^l_{i+1/2,j}$ at the cell interface $x_{i+1/2,j}$, here we set $x_{i+1/2,j}=0$ for all the following reconstruct polynomials, and for the domain $[-1,0]$, the zero-mean form polynomials are given by

$$\begin{aligned}
&Z_0(x)=1,\\
&Z_1(x)=\frac{1}{\Delta x}x-\frac{1}{2}, \quad Z_2(x)=\frac{1}{\Delta x^2}x^2+\frac{1}{3}, \quad Z_3(x)=\frac{1}{\Delta x^3}x^3-\frac{1}{4}, \quad Z_4(x)=\frac{1}{\Delta x^4}x^4+\frac{1}{5},\\
&Z_5(x)=\frac{1}{\Delta x^5}x^5-\frac{1}{6}, \quad Z_6(x)=\frac{1}{\Delta x^6}x^6+\frac{1}{7}, \quad Z_7(x)=\frac{1}{\Delta x^7}x^7-\frac{1}{8}, \quad Z_8(x)=\frac{1}{\Delta x^8}x^8+\frac{1}{9}.
\end{aligned}$$

3.1 Discontinuity feedback factor

To deal with the possible discontinuities in the flow field, Ji et al. [16, 37] proposed an indicator for feedback on the strength of the interface discontinuity based on the reconstructed values of the interface, which is called the discontinuity feedback factor (DF). The effect of DF is that when there exist discontinuities in the reconstruction stencil, the nth-order reconstruction polynomial will be automatically reduced to the 1st-order reconstruction, thus improving the robustness of the algorithm.

To capture the discontinuity more effectively, the improved DF is considered. First, we calculate the discontinuity strength $\sigma_{j+1/2}$ at the interface $\Gamma_{j+1/2}$

$$\sigma_{j+1/2}=\mathbf{Avg}\left\{\sum_{m=1}^{n}\sigma_{j+1/2,m}\right\}, \tag{3.1}$$

where $\sigma_{j+1/2}\geq 0$, and $\sigma_{j+1/2,m}$ is the discontinuity strength of the mth Gauss point at the interface $\Gamma_{j+1/2}$, which has the form

$$\sigma_{j+1/2,m}=\frac{|p^l-p^r|}{p^l}+\frac{|p^l-p^r|}{p^r}+\left(\mathrm{Ma}^l_n-\mathrm{Ma}^r_n\right)^2+\left(\mathrm{Ma}^l_t-\mathrm{Ma}^r_t\right)^2, \tag{3.2}$$

where $\rho^k, k=l,r$ denote the left and right density of the Gauss point $x_{j+1/2.m}$, $p^k, k=l,r$ denote the left and right pressure of the Gauss point $x_{j+1/2.m}$, Ma^l_n, Ma^l_t denote the left Mach number defined by the normal and tangential velocity, respectively.

Remark 3.1. The $\sigma_{j+1/2}$ corresponds to the strength of the discontinuity. As long as the $\sigma_{j+1/2}=0$, the flow is smooth. However, the numerical solution itself is not strictly continuous, which means that some interfaces have a $\sigma_{j+1/2}$ of slightly larger than 0, which corresponds to the weak discontinuities and can be dissipated during reconstruction, i.e. redundant reconstruction polynomial modifications. To deal with the problem, we set a threshold σ_{thres} for the $\sigma_{j+1/2}$, which is used to determine whether there is a discontinuity at the interface. The closer the threshold is to 0, the more reconstruction polynomials will be modified by DF. To improve the robustness and maintain the high resolution of the algorithm, a threshold σ_{thres} is used in this paper, which means $\cdots+\sigma_{j-3/2}+\sigma_{j-1/2}+\sigma_{j+1/2}+\sigma_{j+3/2}+\cdots=0$ when $\cdots+\sigma_{j-3/2}+\sigma_{j-1/2}+\sigma_{j+1/2}+\sigma_{j+3/2}+\cdots<\sigma_{thres}$. The choice of σ_{thres} will be analyzed in Section 4.1.

Second, we need to calculate the DF factor α_S

$$\begin{aligned} &A=\cdots+\sigma_{j-3/2}+\sigma_{j-1/2}+\sigma_{j+1/2}+\sigma_{j+3/2}+\cdots,\\ &\alpha_S=\begin{cases} 1.0 & \text{if } A<\sigma_{thres},\\ \frac{\sigma_{thres}}{\cdots+\sigma_{j-3/2}+\sigma_{j-1/2}+\sigma_{j+1/2}+\sigma_{j+3/2}+\cdots} & \text{otherwise,} \end{cases} \end{aligned} \tag{3.3}$$

where $\alpha_S\in(0,1]$ is the DF factor of the stencil S. When $\alpha_S=1$, which means the stencil is smooth, when $\alpha_S\to 0$, there are strong discontinuities in the stencil. $\{\cdots+\sigma_{j-3/2}+\sigma_{j-1/2}+\sigma_{j+1/2}+\sigma_{j+3/2}+\cdots\}$ is the sum discontinuity strength of all interfaces in a given direction in the stencil.

Remark 3.2. For the normal and tangential reconstruction of the cell $\Omega_{i,j}$, it is necessary to calculate the DF of the corresponding direction of the stencil. As shown in Fig. 1, taking the x-direction as an example, $\{\cdots+\sigma_{i-3/2,j}+\sigma_{i-1/2,j}+\sigma_{i+1/2,j}+\sigma_{i+3/2,j}+\cdots\}$ is considered in the normal reconstruction, and $\{\cdots+\sigma_{i,j-3/2}+\sigma_{i,j-1/2}+\sigma_{i,j+1/2}+\sigma_{i,j+3/2}+\cdots\}$ is considered in the tangential reconstruction.

3.2 ASE-DF(5,3)

First we introduce the WENOZ-AO(5,3) method. The key idea of the 5th-order WENOZ-AO method is to reconstruct a reliable polynomial based on three 3rd-order sub-stencils $\{S^{r3}_{-1},S^{r3}_{0},S^{r3}_{1}\}$ and a 5th-order stencil S^{r5} [1,3], which can obtain the 5th-order accuracy in the smooth region. Consider the variables $\{W_{-2},W_{-1},W_0,W_1,W_2\}$, the stencil S^{r3}_{-1} gives

$$W_{x1}=2W_0-3W_{-1}+W_{-2},\quad W_{x2}=\frac{1}{2}(W_{-2}-2W_{-1}+W_0).$$

The stencil S^{r3}_{0} gives

$$W_{x1}=W_1-W_0,\quad W_{x2}=\frac{1}{2}(W_{-1}-2W_0+W_1).$$

The stencil S^{r3}_{1} gives

$$W_{x1}=W_1-W_0,\quad W_{x2}=\frac{1}{2}(W_0-2W_1+W_2).$$

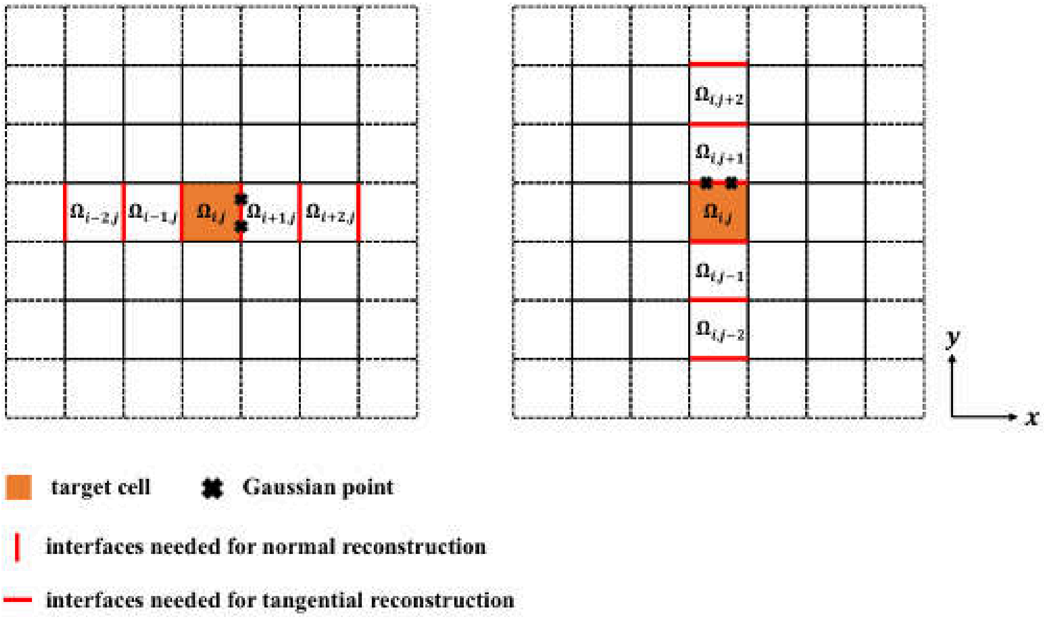

Figure 1: 5th order reconstruction (x-direction, two Gaussian points are used) at the left side of the interface $\Gamma_{i+1/2,j}$. Discontinuity strength of the interfaces to be considered for normal and tangential reconstruction(from left to right).

The stencil S^{r5} gives

$$W_{x1}=\frac{1}{12}(-15W_0+W_{-1}+15W_1-W_2),\quad W_{x_2}=\frac{1}{8}(-8W_0+6W_{-1}-W_{-2}+2W_1+W_2),$$
$$W_{x3}=\frac{1}{6}(3W_0-W_{-1}-3W_1+W_2),\quad W_{x4}=\frac{1}{24}(6W_0-4W_{-1}+W_{-2}-4W_1+W_2).$$

To deal with the discontinuity, the WENOZ type non-linear weights are used as

$$\omega_k=d_k\left(1+\frac{\tau_Z^2}{(\beta_k+\varepsilon)^2}\right), \tag{3.4}$$

where $\varepsilon=10^{-6}$, d_k are the linear weights, and have the following values

$$d_0^5=d_{Hi},\ d_{-1}^3=(1-d_{Hi})(1-d_{Lo})/2,\quad d_0^3=(1-d_{Hi})d_{Lo},\ d_1^3=d_{-1}^3.$$

Here $d_{Hi}=d_{Lo}=0.85$ are used. The global smoothness indicator τ_Z is defined as

$$\tau_Z=\frac{1}{3}(|\beta_0^5-\beta_{-1}^3|+|\beta_0^5-\beta_1^3|+|\beta_0^5-\beta_1^3|).$$

The local smoothness indicators are defined as

$$\beta_k=\sum_{q=1}^{q_k}\Delta x^{2q-1}\int_{x_{i-1/2,j}}^{x_{i+1/2,j}}\left(\frac{\mathrm{d}^q}{\mathrm{d}x^q}\mathrm{P}_k(x)\right)^2\mathrm{d}x, \tag{3.5}$$

where q_k is the order of $\mathrm{P}_k(x)$. However, the calculation of the smoothness indicator is a heavy part of the whole reconstruction, for the WENOZ-AO reconstruction, not only β_k^3, $k=-1,0,1$ but also β_0^5 need to be calculated, and Huang et al. [14] found the computational cost of β_0^5 is comparable with the sum of one of all β_k^3, $k=-1,0,1$. To improve the computational efficiency of the algorithm, here we use a simple smoothness indicator $\overline{\beta}_0^5$ [20] to replace the initial β_0^5 for $\mathrm{P}^{r5}(x)$

$$\overline{\beta}_0^5=\frac{1}{6}\left(\beta_{-1}^3+4\beta_0^3+\beta_1^3\right)+|\beta_{-1}^3-\beta_1^3|. \tag{3.6}$$

Remark 3.3. To verify the consistency of the simplified $\overline{\beta_0^5}$ with the initial β_0^5, using the Taylor expansion of W at x_i, we can obtain

$$\begin{cases}\beta_{-1}^3=(W')^2\Delta x^2+\left(\frac{13}{12}(W'')^2-\frac{2}{3}W'W'''\right)\Delta x^4+\mathcal{O}(\Delta x^5),\\ \beta_0^3=(W')^2\Delta x^2+\left(\frac{13}{12}(W'')^2+\frac{1}{3}W'W'''\right)\Delta x^4+\mathcal{O}(\Delta x^5),\\ \beta_1^3=(W')^2\Delta x^2+\left(\frac{13}{12}(W'')^2-\frac{2}{3}W'W'''\right)\Delta x^4+\mathcal{O}(\Delta x^5),\\ \beta_0^5=(W')^2\Delta x^2+\frac{13}{12}(W'')^2\Delta x^4+\mathcal{O}(\Delta x^5),\end{cases}$$

whereas for smoothness indicator $\overline{\beta_0^5}$, we have

$$\overline{\beta}_0^5=(W')^2\Delta x^2+\frac{13}{12}(W'')^2\Delta x^4+\mathcal{O}(\Delta x^5), \tag{3.7}$$

which is exactly same as β_0^5 upto truncation error level of order $\mathcal{O}(\Delta x^5)$.

Then, the global smoothness indicator τ_Z is modified as

$$\tau_Z=\frac{1}{3}(|\overline{\beta}_0^5-\beta_{-1}^3|+|\overline{\beta}_0^5-\beta_1^3|+|\overline{\beta}_0^5-\beta_1^3|).$$

The ASE-DF method is to use DF factor to automatically select the appropriate stencils for reconstruction, and can be easily generalized to arbitrary high-order methods. The DF factor reflects the strength of the discontinuity in the stencil, and we consider the stencil to be smooth when $\alpha_{\mathrm{S}^{r5}}=1$, then we directly use the linear 5th-order polynomial reconstruction, which has the form

$$\mathbb{P}_{DF}(x)=W_0+W_{x1}Z_1(x)+W_{x2}Z_2(x)+W_{x3}Z_3(x)+W_{x4}Z_4(x), \tag{3.8}$$

when $\alpha_{\mathrm{S}^{r5}}<1$, it is necessary to fall back to the WENOZ-AO method, and to enhance the robustness of the algorithm, combined with the DF factor $\alpha_{\mathrm{S}_i^{r3}},\alpha_{\mathrm{S}^{r5}}$, the ith reconstructed polynomial can be expressed as

$$\begin{aligned}&\mathbb{P}_i^{\prime 3}(x)=W_0+\alpha_{\mathrm{S}_i^{r3}}\left[W_{x1}Z_1(x)+W_{x2}Z_2(x)\right],\\ &\mathbb{P}^{\prime 5}(x)=W_0+\alpha_{\mathrm{S}^{r5}}\left[W_{x1}Z_1(x)+W_{x2}Z_2(x)+W_{x3}Z_3(x)+Z_4(x)\right].\end{aligned}$$

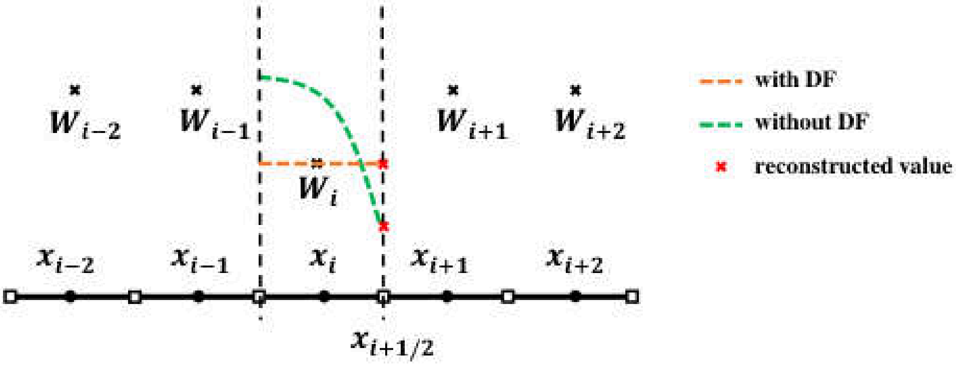

Figure 2: A possible distribution of variables $\{W_{i-2},W_{i-1},W_i,W_{i+1},W_{i+2}\}$. Each sub-stencil has a discontinuity, and the WENO reconstruction can only select the relatively smooth sub-stencil by weights. Take stencil $\{W_{i-2},W_{i-1},W_i\}$ as an example, the green line shows the reconstructed polynomial in the domain $[x_{i-1/2},x_{i+1/2}]$ by WENO method, and the orange line shows the DF factor can automatically converge the reconstructed polynomial to 1st-order when stencil exist a discontinuity, which is more robust compared to the WENO method.

Combined with the normalized weights $\overline{\omega}_k=\omega_k/\sum\omega_k$, the final form of the reconstructed polynomial is

$$\mathbb{P}_{DF}(x)=\overline{\omega}_0^5\left(\frac{1}{d_0^5}\mathbb{P}^{r5}(x)-\sum_{k=-1}^{1}\frac{d_k^3}{d_0^5}\mathbb{P}_k^{r3}(x)\right)+\sum_{k=-1}^{1}\overline{\omega}_k^3\mathbb{P}_k^{r3}(x). \tag{3.9}$$

Remark 3.4. When $\alpha_S\to 1$, the reconstructed polynomial will revert to the initial smooth polynomial, when $\alpha_S\to 0$, which means there exists strong discontinuity in the stencil, and the reconstructed polynomial will be down to 1st-order, i.e. $\mathbb{P}(x)\approx W_0$. As shown in Fig. 2, α_S can handle extreme cases that cannot be handled by the WENO scheme, thus improving the robustness of the algorithm.

3.3 ASE-DF(7,5,3)

The stencil S^{r7} gives

$$\begin{aligned}
W_{x1}&=\frac{1}{180}(-245W_0+25W_{-1}-2W_{-2}+245W_1-25W_2+2f_3),\\
W_{x2}&=\frac{1}{240}(-230W_0+210W_{-1}-57W_{-2}+7W_{-3}+15W_1+63W_2-8W_3),\\
W_{x3}&=\frac{1}{36}(28W_0-11W_{-1}+W_{-2}-28W_1+11W_2-W_3),\\
W_{x4}&=\frac{1}{144}(46W_0-39W_{-1}+15W_{-2}-2W_{-3}-24W_1+3W_2+W_3),
\end{aligned}$$

$$W_{x5}=\frac{1}{120}(-10W_0+5W_{-1}-W_{-2}+10W_1-5W_2+W_3),$$
$$W_{x6}=\frac{1}{720}(-20W_0+15W_{-1}-6W_{-2}+W_{-3}+15W_1-6W_2+W_3).$$

When $\alpha_{\mathbb{S}'^5}=1$, which means that the stencil is smooth, we try to extend the two cells $\{W_{-3},W_3\}$ to get the stencil $\mathbb{S}'^7=\{W_{-3},W_{-2},W_{-1},W_0,W_1,W_2,W_3\}$. Calculate the DF factor $\alpha_{\mathbb{S}'^7}$ of the stencil $\mathbb{S}'^7$ by Eq. (3.3), when $\alpha_{\mathbb{S}'^7}=1$, which implies that $\mathbb{S}'^7$ is also smooth, then we directly use the linear 7th-order polynomial reconstruction, which has the form

$$\mathbb{P}_{DF}(x)=W_0+W_xZ_1(x)+W_{x2}Z_2(x)+W_{x3}Z_3(x)+W_{x4}Z_4(x)+W_{x5}Z_5(x)+W_{x6}Z_6(x), \tag{3.10}$$

when $\alpha_{\mathbb{S}'^7}<1$, the reconstruction will fall back to ASE-DF(5,3). Compared with the classical WENO method, the ASE-DF does not require additional calculation of the smoothness indicator, which significantly improves computational efficiency.

3.4 ASE-DF(9,7,5,3)

The stencil $\mathbb{S}'^9$ gives

$$\begin{aligned}
W_{x1}=&\frac{1}{5040}(-7175W_0+889W_{-1}-119W_{-2}+9W_{-3}+7175W_1-889W_2+119W_3-9W_4),\\
W_{x2}=&\frac{1}{30240}(-27895W_0+28679W_{-1}-9835W_{-2}+2081W_{-3}-205W_{-4}-2065W_1\\
&+11459W_2-2455W_3+236W_4),\\
W_{x3}=&\frac{1}{1440}(1365W_0-587W_{-1}+89W_{-2}-7W_{-3}-1365W_1+587W_2-89W_3+7W_4),\\
W_{x4}=&\frac{1}{3456}(1174W_0-1160W_{-1}+556W_{-2}-128W_{-3}+13W_{-4}-464W_1-68W_2\\
&+88W_3-11W_4),\\
W_{x5}=&\frac{1}{480}(-75W_0+41W_{-1}-11W_{-2}+W_{-3}+75W_1-41W_2+11W_3-W_4),\\
W_{x6}=&\frac{1}{8640}(-380W_0+334W_{-1}-170W_{-2}+46W_{-3}-5W_{-4}+250W_1-86W_2+10W_3+W_4),\\
W_{x7}=&\frac{1}{5040}(35W_0-21W_{-1}+7W_{-2}-W_{-3}-35W_1+21W_2-7W_3+W_4),\\
W_{x8}=&\frac{1}{40320}(70W_0-56W_{-1}+28W_{-2}-8W_{-3}+W_{-4}-56W_1+28W_2-8W_3+W_4).
\end{aligned}$$

Similarly to ASE-DF(7,5,3), when $\alpha_{\mathbb{S}'^7}=1$, we try to further expand the stencil and obtain the stencil $\mathbb{S}'^9$. Calculate the DF factor $\alpha_{\mathbb{S}'^9}$ by Eq. (3.3), when $\alpha_{\mathbb{S}'^9}=1$, then we directly use the linear 9th-order polynomial reconstruction, which has the form

$$\begin{aligned}
\mathbb{P}_{DF}(x)=&W_0+W_xZ_1(x)+W_{x2}Z_2(x)+W_{x3}Z_3(x)+W_{x4}Z_4(x)\\
&+W_{x5}Z_5(x)+W_{x6}Z_6(x)+W_{x7}Z_7(x)+W_{x8}Z_8(x),
\end{aligned}\tag{3.11}$$

when $\alpha_{S^{r9}} < 1$, the reconstruction will fall back to ASE-DF(7,5,3).

By expanding the stencil, we can easily obtain arbitrary higher-order reconstruction methods. The ASE-DF algorithm for selecting stencils is shown in Algorithm 1.

Algorithm 1: DF-based adaptive stencil extension reconstruction methods

```
Input: Interfaces reconstructed values $\mathbf{W}^l, \mathbf{W}^r$.
Output: The needed stencil S for the reconstruction.
calculate the correspond DF values $\alpha^{r5} \leftarrow (\mathbf{W}^l, \mathbf{W}^r)$ by Eq. (3.3).
if $\alpha^{r5} < 1$ then
    select the non-linear WENOZ-AO(5,3) with DF reconstruction method;
else
    calculate the correspond DF values $\alpha^{r7} \leftarrow (\mathbf{W}^l, \mathbf{W}^r)$ by Eq. (3.3).
    if $\alpha^{r7} < 1$ then
        select the linear 5th-order polynomial reconstruction method;
    else
        calculate the correspond DF values $\alpha^{r9} \leftarrow (\mathbf{W}^l, \mathbf{W}^r)$ by Eq. (3.3).
        if $\alpha^{r9} < 1$ then
            select the linear 7th-order polynomial reconstruction method;
        else
            calculate the correspond DF values $\alpha^{r11} \leftarrow (\mathbf{W}^l, \mathbf{W}^r)$ by Eq. (3.3).
            if $\alpha^{r11} < 1$ then
                select the linear 9th-order polynomial reconstruction method;
            else
                ...
            end
        end
    end
end
return.
```

3.5 Reconstruction of equilibrium state for gas-kinetic scheme

For the non-equilibrium state, the reconstruction can be used to obtain the equilibrium state g^c, g^c_x and g^c_y directly by $g^k_{\mathbf{x}}, k=l,r$, and a kinetic-based weighting method is used

$$\begin{aligned} \int \psi g^c \mathrm{d}\Xi = \mathbf{W}^c = \int_{u>0} \psi g^l \mathrm{d}\Xi + \int_{u<0} \psi g^r \mathrm{d}\Xi, \\ \int \psi g^c_{\mathbf{x}} \mathrm{d}\Xi = \mathbf{W}^c_{\mathbf{x}} = \int_{u>0} \psi g^l_{\mathbf{x}} \mathrm{d}\Xi + \int_{u<0} \psi g^r_{\mathbf{x}} \mathrm{d}\Xi. \end{aligned} \tag{3.12}$$

In this way, all the variables needed in the algorithm have been determined.

4 Numerical experiments

In this section, ASE-DF reconstruction methods and two flux solvers are used to simulate several inviscid and viscous problems.

4.1 Analysis of the discontinuity threshold σ_{thres}

In our proposed algorithm, the selection of the σ_{thres} is crucial for the calculation of the strong shock wave problems. From Eq. (3.3), it can be seen that when a smaller value of σ_{thres} is chosen, the more reconstruction polynomials will be modified by DF, which leads to more order-reducing of the reconstruction. As a result, the robustness of the whole algorithm is improved but the resolution will be significantly reduced. When a larger value of σ_{thres} is chosen, which means that possible discontinuities in the stencil will not be recognized, and more higher-order smooth stencils will be used, the resolution of the algorithm will be improved, unfortunately, it leads to more pronounced oscillations and the robustness will decrease.

In order to select a suitable σ_{thres}, we present the numerical results of two strong shock wave problems.

Example 4.1 (Blast wave problem). The initial conditions for the blast wave problem are given as follows

$$(\rho,u,p)=\begin{cases}(1,0,1000), & 0\le x\le 0.1,\\(1,0,0.01), & 0.1\le x\le 0.9,\\(1,0,100), & 0.9\le x\le 1.0.\end{cases}$$

400 uniform meshes are used and reflection boundary conditions are applied at both ends. The density distribution at $t=3.8$ is presented in Fig. 3. It can be seen that as

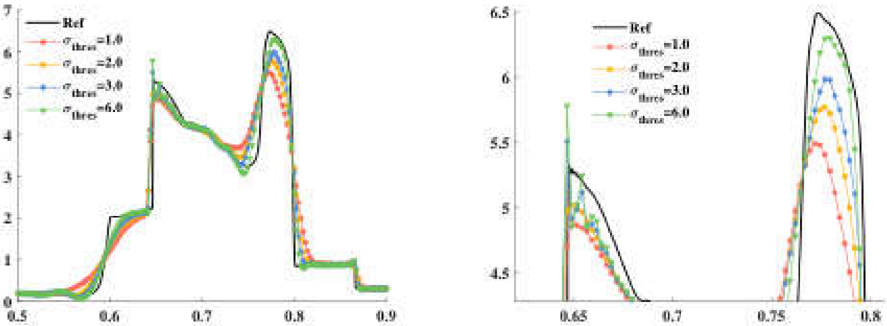

Figure 3: Blast wave problem: the density distributions and local enlargement at $t=3.8$ with a cell size $\Delta x=1/400$. $c_1=0.05$, $c_2=5.0$. Different values of σ_{thres} using the ASE-DF(5,3) with the GKS solver. The reference solution is obtained by the 1-D 5th-order WENO-AO GKS with 4000 meshes.

σ_{thres} increases, the resolution of the algorithm increases with a significant increase in oscillations, while decreases significantly when σ_{thres} is small.

Example 4.2 (Configuration 3). Configuration 3 in [22] involves the shock-shock interaction and shock-vortex interaction. The initial condition in the domain $[0,1]\times[0,1]$ is given by

$$(\rho,u,v,p)=\begin{cases}(0.138,1.206,1.206,0.129), & x<0.7,\ y<0.7,\\(0.5323,0,1.206,0.3), & x\geq 0.7,\ y<0.7,\\(1.5,0,0,1.5), & x\geq 0.7,\ y\geq 0.7,\\(0.5323,1.206,0,0.3), & x<0.7,\ y\geq 0.7.\end{cases}$$

The numerical results are shown in Fig. 4, similar conclusion to blast wave case, further, no significant increase in resolution when σ_{thres} is increasing.

Thus, in order to balance robustness and resolution of the algorithm, we select $\sigma_{thres}=2.0$ in the following numerical simulation.

4.2 Accuracy validations

To test the accuracy of the ASE-DF schemes, the smooth sin-wave propagation [18] is considered. In these cases, both the physical viscosity and the collision time are set to zero. The initial condition of the equation is given by

$$\rho(x)=1+0.2\sin(\pi x),\quad U(x)=1.0,\quad p(x)=1.0,\quad x\in[0,2], \tag{4.1}$$

and the exact solution has the form

$$\rho(x,t)=1.0+0.2\sin(\pi(x-t)),\quad U(x,t)=1.0,\quad p(x,t)=1.0.$$

Periodic boundary condition is used, and the numerical results are obtained after a periodic propagation at $t=2.0$. The accuracy of the schemes are measured in L^1-error norms in the domain $[0,2]$.

Extending to the 2-D case, the initial condition of the 2-D sin-wave propagation is

$$\begin{aligned}&\rho(x,y)=1.0+0.2\sin(\pi x)\sin(\pi y),\\&U(x,y)=1.0,\quad V(x,y)=1.0,\quad p(x,y)=1.0,\end{aligned}$$

with the exact solution

$$\begin{aligned}&\rho(x,y,t)=1.0+0.2\sin(\pi(x-t))\sin(\pi(y-t)),\\&U(x,y,t)=1.0,\quad V(x,y,t)=1.0,\quad p(x,y,t)=1.0.\end{aligned}$$

To maintain the same accuracy in time and space, $dt=dx^{r/s}$ is used, where r corresponds to the spatial order, and s corresponds to the temporal order. The numerical results are shown in Tables 1-2. The results show that the different schemes can achieve their theoretical numerical accuracy.

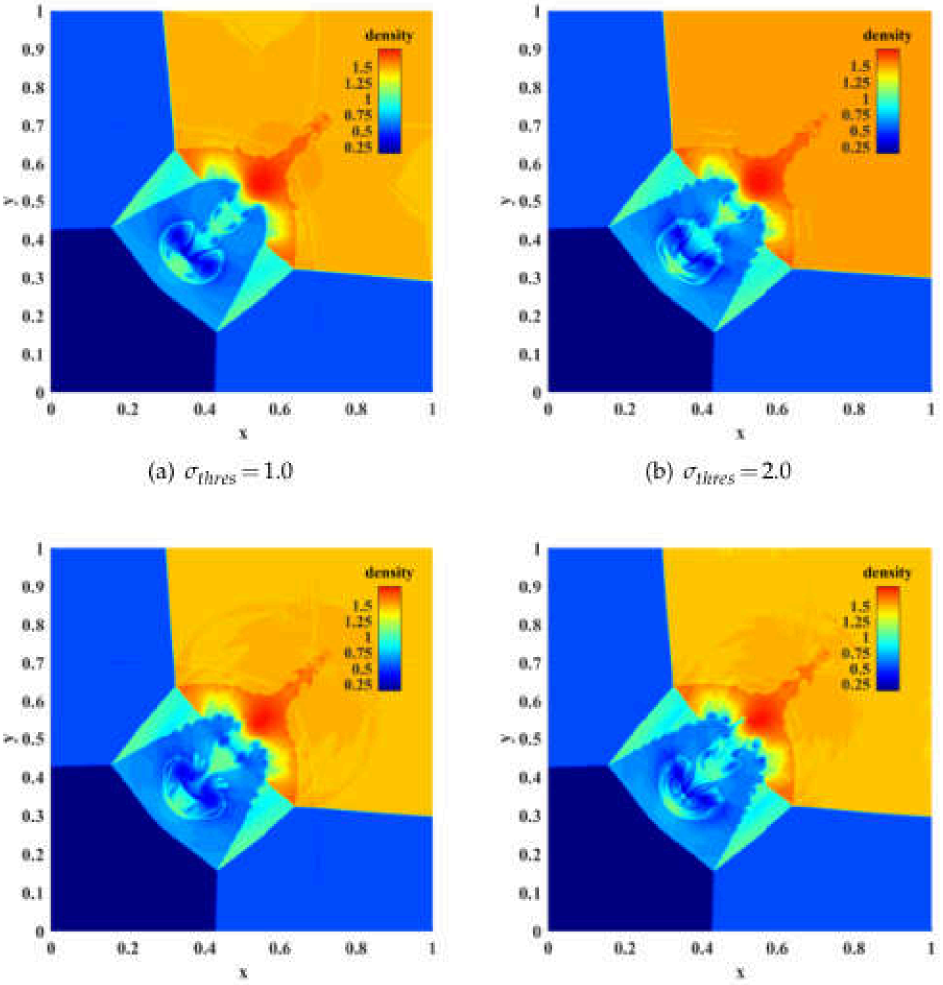

(a) $\sigma_{thres}=1.0$ (b) $\sigma_{thres}=2.0$

(c) $\sigma_{thres}=3.0$ (d) $\sigma_{thres}=6.0$

Figure 4: Configuration 3: the density distribution at $t=0.6$ with 500×500 meshes. $c_1=0.05$, $c_2=1.0$. This figure is drawn with 30 density contours. (a-d) Different values of σ_{thres} using the ASE-DF(5,3) with the GKS solver.

4.3 Test cases with discontinuities

Example 4.3 (Shu-Osher problem). The Shu-Osher problem can examine the performance of capturing high frequency wave, and the initial condition is given by

$$(\rho,u,p)=\begin{cases}(3.857134,2.629369,10.33333), & x\in[0.0,1.0],\\(1.0+0.2\sin(5x),0,1), & x\in[1.0,10.0].\end{cases}$$

Table 1: Accuracy test for the 1-D sin-wave propagation in L^1-error norms.

N	ASP-DF(5,3)	order	ASP-DF(7,5,3)	order	ASP-DF(9,7,5,3)	order
10	8.811260e-04		7.397310e-05		6.481933e-06	
20	2.585904e-05	4.85	6.366042e-07	6.84	1.424192e-08	8.83
40	8.337553e-07	4.95	5.108345e-09	6.96	2.848478e-11	8.97
80	2.680325e-08	4.95	4.042055e-11	6.98	9.085371e-14	8.29

Table 2: Accuracy test for the 2-D sin-wave propagation in L^1-error norms.

N	ASP-DF(5,3)	order	ASP-DF(7,5,3)	order	ASP-DF(9,7,5,3)	order
10×10	1.454911e-03		1.247749e-04		1.797550e-05	
20×20	5.695852e-05	4.74	2.475327e-06	6.94	3.661497e-08	8.94
40×40	1.882335e-06	4.92	1.911540e-08	7.02	8.139979e-11	8.81
80×80	6.106553e-08	4.95	1.490022e-10	7.00	4.792616e-13	7.41

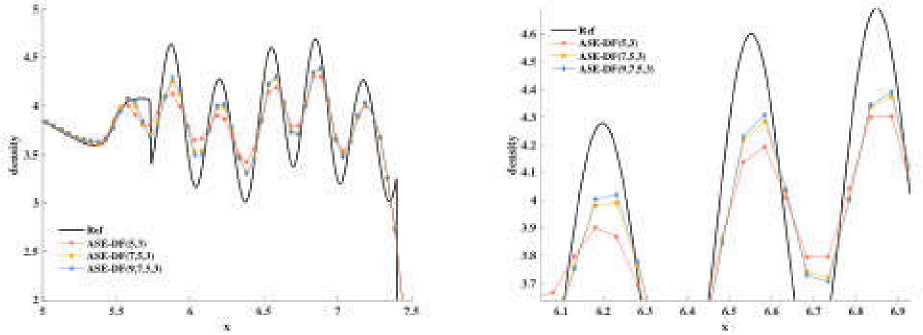

Figure 5: Shu-Osher problem: the density distributions and local enlargement at $t=1.8$ with a cell size $\Delta x=1/20$. All results are calculated by the GKS solver, $c_1=0.05$, $c_2=1.0$. The reference solution is obtained by the 1-D 5th-order WENO-AO GKS with 10000 meshes.

To clearly distinguish the ability of different schemes, 200 meshes are used. A CFL number $\theta_{CFL}=0.5$ is used for the all following cases. Fig. 5 shows the density distribution using the different reconstruction methods, for the same mesh size, both ASE-DF(7,5,3) and ASE-DF(9,7,5,3) perform better in capturing high frequency waves compared to ASE-DF(5,3), which is consistent with theoretical expectations, and limited by the number of meshes, the resolution of ASE-DF(9,7,5,3) is not significantly higher compared to ASE-DF(7,5,3).

Example 4.4 (Blast wave problem). To test the performance of the different reconstruction methods, the blast problem is simulated again. 400 uniform meshes are used and re-

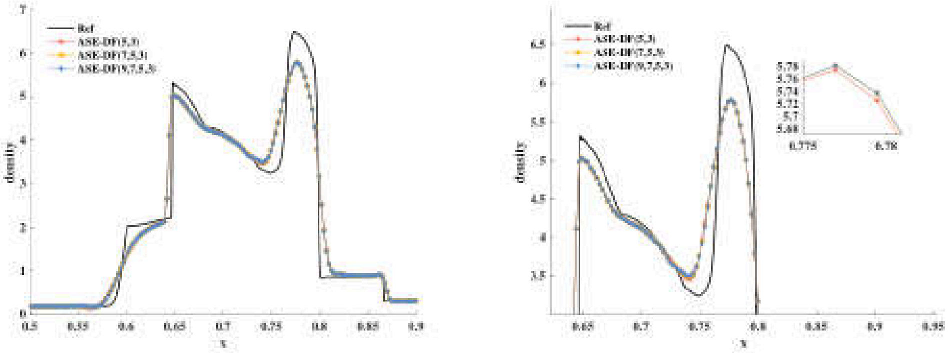

Figure 6: Blast wave problem: the density distributions and local enlargement at $t=3.8$ with a cell size $\Delta x=1/400$. All results are calculated by the GKS solver, $c_1=0.05$, $c_2=5.0$. The reference solution is obtained by the 1-D 5th-order WENO-AO GKS with 4000 meshes.

flection boundary conditions are applied at both ends. The density distribution at $t=3.8$ is presented in Fig. 6. It can be seen that resolution of the algorithm is slightly increasing as the order increases, this is due to the fact that the presence of strong shock waves in this problem, and due to the DF, leads to higher-order reconstruction being treated more significantly by downgrading, i.e., ASE-DF(9,7,5,3) also perform almost identically to ASE-DF(5,3).

Example 4.5 (Configuration 3). The problem has been described in Section 4.1. The numerical results are shown in Fig. 7, all schemes show low-dissipation, and the main differences among all schemes are the strength of the shear layers, both ASE-DF(9,7,5,3) and ASE-DF(7,5,3) are capable of resolving significantly more vortical structures compared to ASE-DF(5,3). It is observed that the symmetry structure obtained by ninth-order ASE-DF L-F scheme is significantly broken in Fig. 7(f), the exact cause remains unclear at present. As reported in [9], successive mathematical operations, especially within the costly root function, lead to a fast amplification of floating-point errors that affects the overall flow evolution even for moderate resolutions. We speculate that this is due to the fact that the L-F flux involves a significant amount of square root and extremum (max/min) operations, which leads to the rapid accumulation of floating-point errors during computation. This, in turn, increases the instability of symmetry. This phenomenon becomes more pronounced in higher-order schemes.

Example 4.6 (double Mach reflection problem). In the double Mach reflection problem [33], a rightwards-moving shock wave at Mach 10 with an incident angle of 60° with respect to the x-axis interacting with a reflection wall boundary, which can test the shock wave capture capability, numerical stability, dissipation and resolution of the scheme.

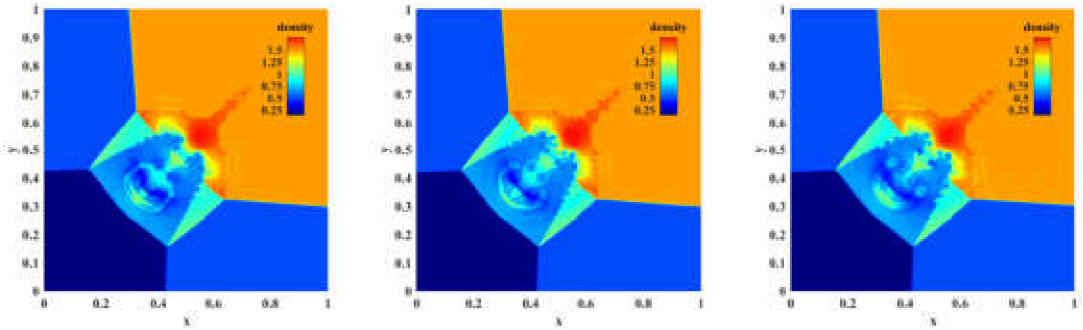

(a) ASE-DF(5,3), GKS solver (b) ASE-DF(7,5,3), GKS solver (c) ASE-DF(9,7,5,3), GKS solver

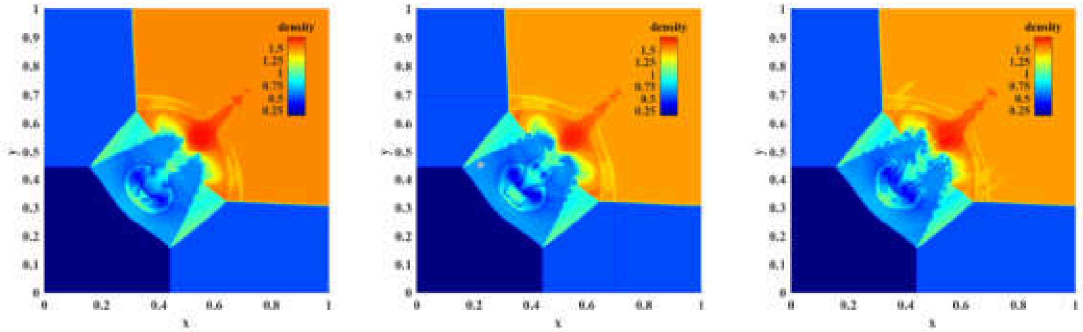

(d) ASE-DF(5,3), L-F solver (e) ASE-DF(7,5,3), L-F solver (f) ASE-DF(9,7,5,3), L-F solver

Figure 7: Configuration 3: the density distribution at $t=0.6$ with 500×500 meshes. This figure is drawn with 30 density contours. (a-c) The results are calculated by the GKS solver. $c_1=0.05$, $c_2=1.0$. (d-f) The results are calculated by the L-F solver.

The initial condition is given by

$$(\rho,u,v,p)=\begin{cases}(1.4,0,0,1), & y<1.732(x-0.1667),\\(8,7.145,-4.125,116.8333), & \text{ohterwise}.\end{cases}$$

The slip boundary condition is used at the wall starting from $x=1/6$, the bottom boundary condition is the post-shock condition. The computational domain is $[0,4]\times[0,1]$, and the numerical results in $[2,3]\times[0,1]$ for all schemes at $t=0.2$ are shown in Fig. 8, which can be observed that all schemes show low-dissipation and can capture the shock wave well.

Example 4.7 (Viscous sod shock problem). For N-S solver, the viscous shock tube problem [8] is considered to test the validity of the scheme. The initial condition in the domain

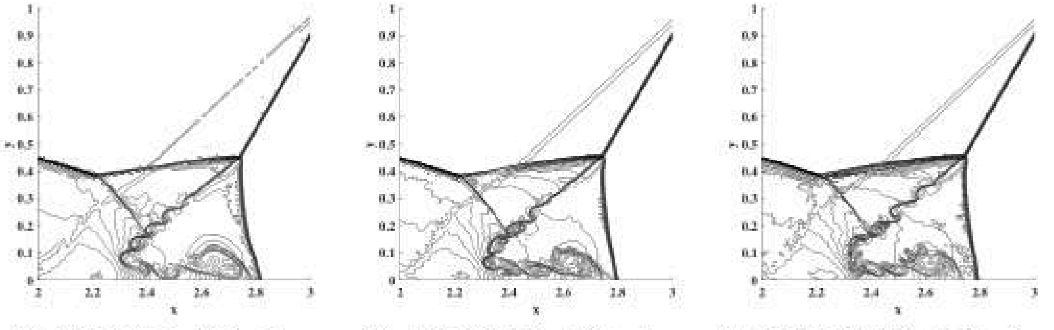

(a) ASE-DF(5,3), GKS solver (b) ASE-DF(7,5,3), GKS solver (c) ASE-DF(9,7,5,3), GKS solver

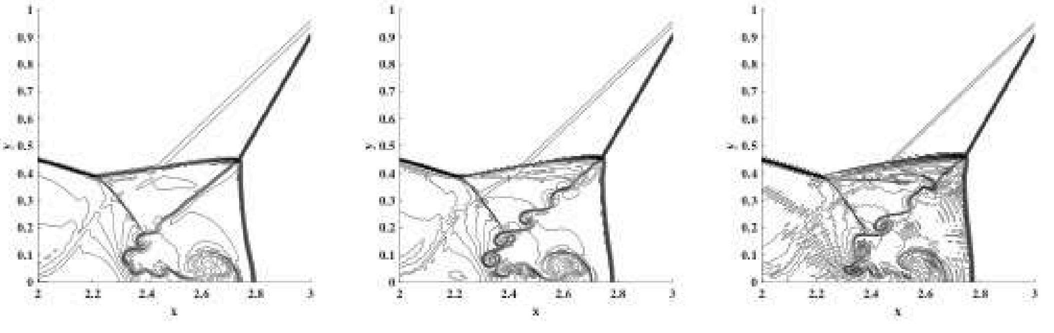

(d) ASE-DF(5,3), L-F solver (e) ASE-DF(7,5,3), L-F solver (f) ASE-DF(9,7,5,3), L-F solver

Figure 8: Double Mach reflection problem: the density distribution at $t=0.2$ with 960×240 meshes. This figure is drawn with 35 density contours. (a-c) The results are calculated by the GKS solver. $c_1=0.05, c_2=1.0$. (d-f) The results are calculated by the L-F solver.

$[0,1]\times[0,0.5]$ is given by

$$(\rho,u,v,p)=\begin{cases}(120,0,0,120/\gamma), & 0<x<0.5,\\(1.2,0,0,1.2/\gamma), & 0.5\leq x<1,\end{cases}$$

where $\gamma=1.4$ and the Prandtl number $Pr=1$. The top boundary is set as a symmetric boundary condition and no-slip adiabatic condition is used for others. For the case $Re=200$, the density distributions with different uniform mesh points at $t=1.0$ from different reconstruct methods are shown in Fig. 9. The density profiles along the lower wall for this case are presented in Fig. 10. As shown in Table 3, the height of primary vortex predicted by the current schemes agree well with the reference data [15].

Example 4.8 (High-mach number astrophysical jet). To test the robustness of the schemes, the high-mach number astrophysical jet [36] is simulated. A low mach number $Ma\approx80$ and a very high mach number $Ma\approx20000$ are considered. The computational

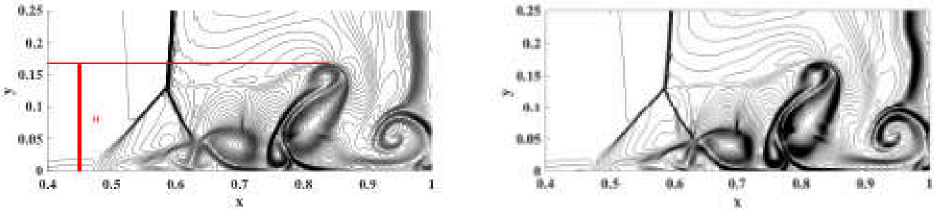

(a) ASE-DF(5,3), $\Delta x = \Delta y = 1/500$ (b) ASE-DF(5,3), $\Delta x = \Delta y = 1/1000$

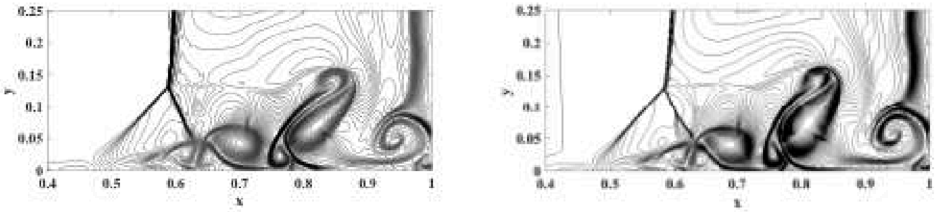

(c) ASE-DF(7,5,3), $\Delta x = \Delta y = 1/500$ (d) ASE-DF(7,5,3), $\Delta x = \Delta y = 1/1000$

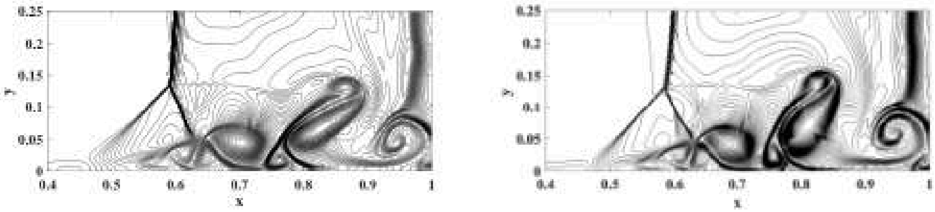

(e) ASE-DF(9,7,5,3), $\Delta x = \Delta y = 1/500$ (f) ASE-DF(9,7,5,3), $\Delta x = \Delta y = 1/1000$

Figure 9: Viscous sod shock problem: the density distribution at $t = 1.0$ for $Re = 200$ case. Left: different reconstruct methods with 500×250 uniform meshes. Right: different reconstruct methods with 1000×500 uniform meshes. All results are calculated by the GKS solver, $c_1 = 1.0, c_2 = 10.0$.

Table 3: Viscous shock tube problem: comparison of the primary vortex heights among different schemes for Re = 200 case. The reference data can be found in [15].

Scheme	S2O4 GKS	S2O4 CGKS	ASP-DF(5,3)	ASP-DF(7,5,3)
Mesh size	500×250	500×250	500×250	500×250
Height	0.171	0.173	0.167	0.163
Scheme	ASP-DF(9,7,5,3)	ASP-DF(5,3)	ASP-DF(7,5,3)	ASP-DF(9,7,5,3)
Mesh size	500×250	1000×500	1000×500	1000×500
Height	0.153	0.171	0.164	0.160

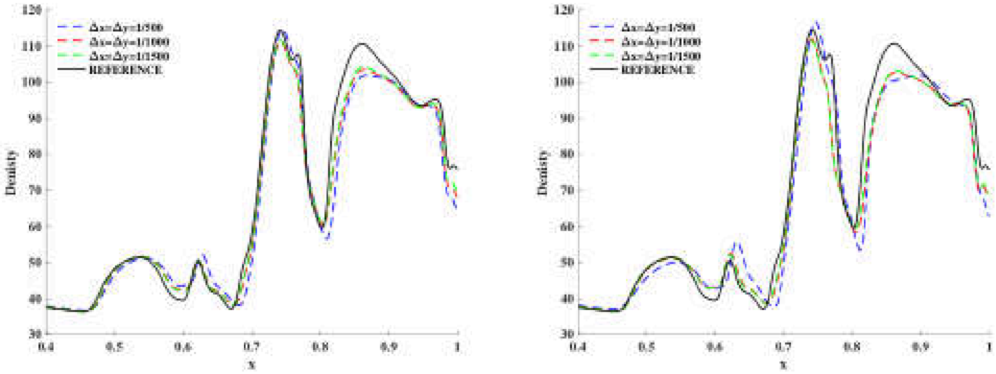

(a) ASE-DF(5,3) (b) ASE-DF(7,5,3)

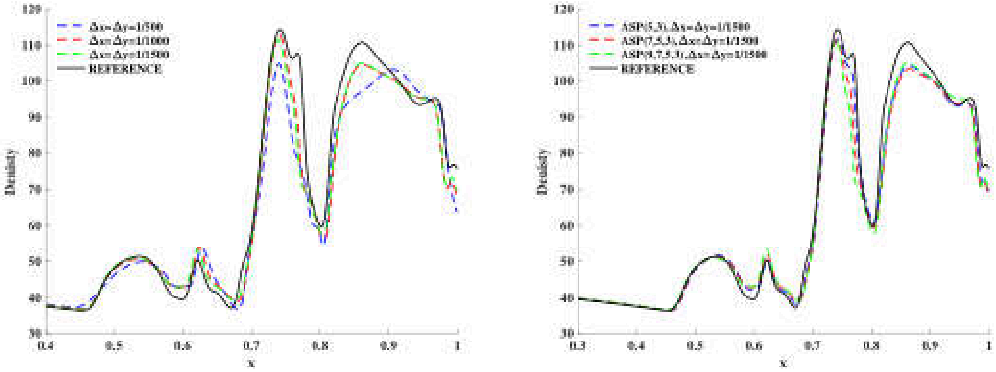

(c) ASE-DF(9,7,5,3) (d) Comparison results

Figure 10: Viscous sod shock problem: density profiles along the lower wall at $t=1.0$ for $Re=200$ case. (a-c) Mesh refinement results for different reconstruct methods. (d) Comparison of different reconstruct methods with 1500×750 uniform meshes. The reference line is obtained from [15].

domain $[0,2]\times[0,1]$ is filled with

$$(\rho,u,v,p,\gamma)=(0.5,0,0,0.4127,5/3).$$

The boundary conditions for the right, top and bottom are outflow. For the left boundary

$$\begin{aligned}(\rho,u,v,p)&=(5,30,0,0.4127), \text{ if } y\in[0.45,0.55] \quad \text{for Ma 80 case,}\\ (\rho,u,v,p)&=(5,8000,0,0.4127), \text{ if } y\in[0.45,0.55] \quad \text{for Ma 20000 case.}\end{aligned}$$

For the Ma 80 case, the terminal time is 0.07, the computation is performed on a 400×200 mesh, and for the Ma 20000 case, the terminal time is 10^{-4}, the computation is performed

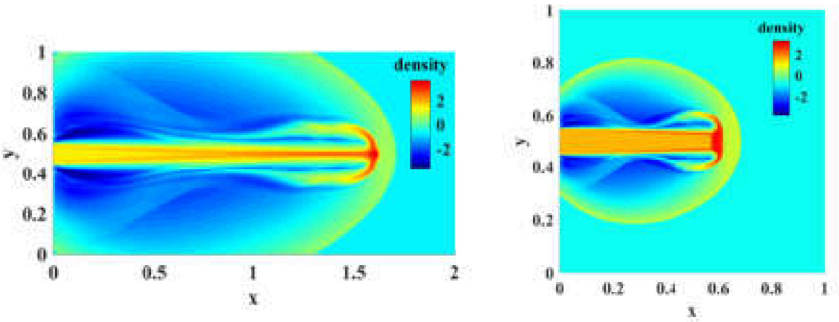

(a) ASE-DF(5,3), Mach 80 (b) ASE-DF(5,3), Mach 20000

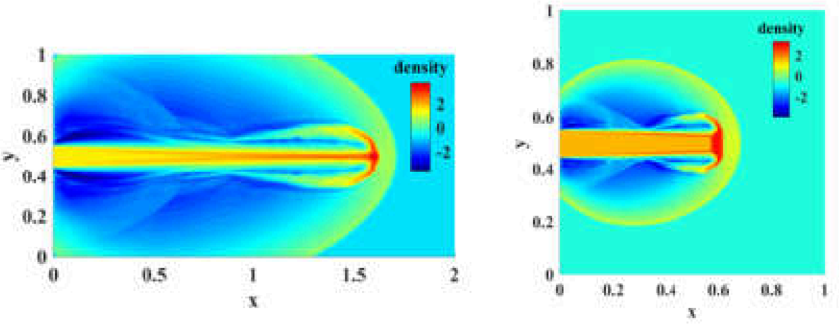

(c) ASE-DF(7,5,3), Mach 80 (d) ASE-DF(7,5,3), Mach 20000

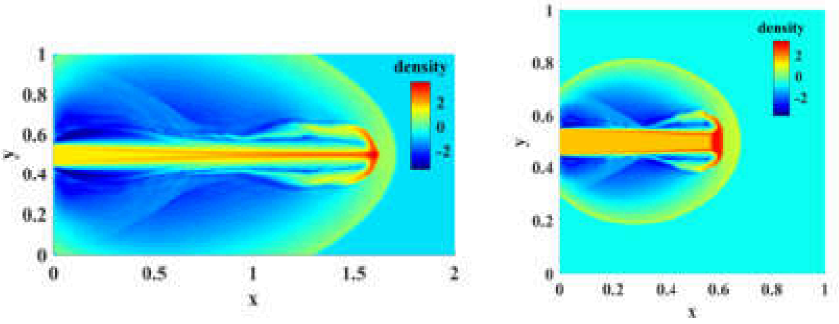

(e) ASE-DF(9,7,5,3), Mach 80 (f) ASE-DF(9,7,5,3), Mach 20000

Figure 11: High-mach number astrophysical jet: the density distribution at $t=0.07$ and $t=10^{-4}$(from left to right). This figure is drawn with 30 density contours. Non-linear function of density $\phi=\log(\rho)$ is used. Left: different reconstruction methods with 400×200 meshes. Right: different reconstruction methods with 800×400 meshes. L-F solver is used for all results.

on a 800×400 mesh. Fig. 11 shows the results when using different reconstruction methods, we see that the proposed algorithm can maintain high resolution at lower Mach number, while the algorithm maintains strong robustness at a very high Mach number.

4.4 Computational efficiency

The 2D Riemann problem (Configuration 3 in [22]) with different mesh sizes are tested for the comparison of computation cost, which is shown in Table 4. The CPU times are recorded after running 20 time steps for each reconstruction method with a single processor of Intel Core i7-13700K Processor @3.40GHz.

Based on the Table 4, since there is no need to calculate additional smoothness indicators in higher-order schemes, the computational time of ASE-DF(7,5,3) is about 1.4 times of ASE-DF(5,3) due to the differences in number of Gaussian points and the reconstruct polynomials, and the computational time of ASE-DF(9,7,5,3) is about 1.3 times of ASE-DF(5,3), i.e. our proposed algorithm remains efficient at arbitrary high-order methods. In addition, compared to the classic WENO scheme, the ASP method can save approximately 30% of the computational time, moreover, as the reconstruction order increases, the efficiency improvement of the ASP method becomes more pronounced.

Table 4: Computational time (in seconds) of different reconstruction methods with the GKS solver for the 2-D Riemann problem.

Mesh size	ASP-DF(5,3)	ASP-DF(7,5,3)	ASP-DF(9,7,5,3)
100×100	4.871	6.867	8.683
200×200	18.826	27.590	34.372
400×400	74.108	106.248	136.324
800×800	293.731	425.135	551.060
Mesh size	WENO(5,3)	WENO(7,5,3)	WENO(9,7,5,3)
100×100	5.816	8.446	11.834
200×200	22.916	33.204	46.345
400×400	91.101	131.382	185.049
800×800	361.582	526.504	737.500

5 Conclusion

This paper presents the Adaptive Stencil Extension reconstruction method with Discontinuity Feedback factor (ASE-DF), addressing two critical challenges in high-order WENO schemes: diminishing robustness at higher orders and increased computational costs from smoothness indicator calculations. Building on WENOZ-AO (5,3), the method incorporates a DF factor to enhance robustness while eliminating additional smoothness indicators, using only the stencil's α_S for higher-order extensions. This approach maintains high resolution and computational efficiency, establishing a foundation for future developments of high-order compact schemes.

Acknowledgments

We dedicate this work to the memory of Professor Jiequan Li, whose pioneering contributions to computational fluid dynamics and generous mentorship have deeply influenced this research. His scientific legacy continues to inspire advancement in numerical methods.

The current research is supported by the National Science Foundation of China (12302378, 12172316, 92371201), Hong Kong Research Grant Council (16301222).

A Calculation of GKS flux function

The form of the 2nd-order gas kinetic distribution function at each Gaussian point with a local coordinate **x** in Eq. (2.10) For a 2-D Maxwell's distribution

$$g=\rho\left(\frac{\lambda}{\pi}\right)^{\frac{K+3}{2}} e^{-\lambda\left[(u-U)^2+(v-V)^2+\xi^2\right]}, \tag{A.1}$$

the moment of g is defined as

$$\rho\langle(\cdots)\rangle=\int(\cdots)g\mathrm{d}\Xi, \tag{A.2}$$

the general moment formula becomes

$$\left\langle\left(u^n v^m \xi^{2l}\right)\right\rangle=\langle(u^n)\rangle\langle(v^m)\rangle\left\langle\left(\xi^{2l}\right)\right\rangle,$$

where n,m,l are integers, and the moments of ξ are always even-order because of its symmetrical property. With the integral in the domain $(-\infty,+\infty)$, we have

$$\begin{aligned}
\langle(u^0)\rangle&=1,\\
\left\langle(u^1)\right\rangle&=U,\\
&\cdots\\
\langle(u^{n+2})\rangle&=U\left\langle(u^{n+1})\right\rangle+\frac{n+1}{2\lambda}\langle(u^n)\rangle,
\end{aligned}$$

and

$$\begin{aligned}
\langle(\xi^0)\rangle&=1,\\
\langle(u^2)\rangle&=\frac{K}{2\lambda},\\
&\cdots\\
\left\langle(\xi^{2l})\right\rangle&=\frac{K+2(l-1)}{2\lambda}\left\langle(\xi^{2(l-1)})\right\rangle.
\end{aligned}$$

Integrating terms with Heaviside function, the integral in the domain $(0,+\infty)$ is denoted as $\langle(\cdots)\rangle_{>0}$, and $(-\infty,0)$ as $\langle(\cdots)\rangle_{<0}$

$$\begin{aligned}
\langle(u^0)\rangle_{>0} &= \frac{1}{2}\mathrm{erfc}\left(-\sqrt{\lambda}U\right),\\
\left\langle(u^1)\right\rangle_{>0} &= U\langle(u^0)\rangle_{>0} + \frac{1}{2}\frac{e^{-\lambda U^2}}{\sqrt{\pi\lambda}},\\
&\cdots\\
\langle(u^{n+2})\rangle_{>0} &= U\left\langle(u^{n+1})\right\rangle_{>0} + \frac{n+1}{2\lambda}\langle(u^n)\rangle_{>0},
\end{aligned}$$

and

$$\begin{aligned}
\langle(u^0)\rangle_{<0} &= \frac{1}{2}\mathrm{erfc}\left(\sqrt{\lambda}U\right),\\
\left\langle(u^1)\right\rangle_{<0} &= U\langle(u^0)\rangle_{<0} - \frac{1}{2}\frac{e^{-\lambda U^2}}{\sqrt{\pi\lambda}},\\
&\cdots\\
\langle(u^{n+2})\rangle_{<0} &= U\left\langle(u^{n+1})\right\rangle_{<0} + \frac{n+1}{2\lambda}\langle(u^n)\rangle_{<0},
\end{aligned}$$

where erfc is the standard complementary error function.

For the Taylor expansion of a Maxwell's distribution, all microscopic derivatives have the form

$$\begin{aligned}
a_x &= a_{x1} + a_{x2}u + a_{x3}v + a_{x4}\frac{1}{2}(u^2+v^2+\xi^2) = a_{xi}\psi_i,\\
a_y &= a_{y1} + a_{y2}u + a_{y3}v + a_{y4}\frac{1}{2}(u^2+v^2+\xi^2) = a_{yi}\psi_i,\\
A &= A_1 + A_2u + A_3v + A_4\frac{1}{2}(u^2+v^2+\xi^2) = A_i\psi_i.
\end{aligned}$$

Combine with Eq. (A.2) and Eq. (2.12), we have

$$\int \psi a_x g \,\mathrm{d}\Xi = \frac{\partial \mathbf{W}}{\partial x}, \tag{A.3}$$

which can be expanded as

$$\begin{pmatrix} b_1\\ b_2\\ b_3\\ b_4 \end{pmatrix} = \frac{1}{\rho}\frac{\partial \mathbf{W}}{\partial x} = \frac{1}{\rho}\begin{pmatrix} \frac{\partial\rho}{\partial x}\\ \frac{\partial(\rho U)}{\partial x}\\ \frac{\partial(\rho V)}{\partial x}\\ \frac{\partial(\rho E)}{\partial x} \end{pmatrix} = \langle(a_{xi}\psi_i\psi_j)\rangle = \langle(\psi_i\psi_j)\rangle\begin{pmatrix} a_{x1}\\ a_{x2}\\ a_{x3}\\ a_{x4} \end{pmatrix}. \tag{A.4}$$

Denoting $\mathbf{M} = \langle(\psi_i\psi_j)\rangle$, the above equations can be expressed as

$$\mathbf{M}\mathbf{a} = \mathbf{b}.$$

For the 2-D case, the coefficient matrix **M** can be expanded as

$$\mathbf{M}=\begin{pmatrix} \langle(u^0)\rangle & \langle(u^1)\rangle & \langle(v^1)\rangle & \langle(\psi_4)\rangle \\ \langle(u^1)\rangle & \langle(u^2)\rangle & \langle(u^1v^1)\rangle & \langle(u^1\psi_4)\rangle \\ \langle(v^1)\rangle & \langle(u^1v^1)\rangle & \langle(v^2)\rangle & \langle(v^1\psi_4)\rangle \\ \langle(\psi_4)\rangle & \langle(u^1\psi_4)\rangle & \langle(v^1\psi_4)\rangle & \langle(\psi_4^2)\rangle \end{pmatrix} =\begin{pmatrix} 1 & U & V & B_1 \\ U & U^2+1/2\lambda & UV & B_2 \\ V & UV & V^2+1/2\lambda & B_3 \\ B_1 & B_2 & B_3 & B_4 \end{pmatrix}, \tag{A.5}$$

where

$$\begin{aligned} B_1&=\frac{1}{2}\left(U^2+V^2+\frac{K+2}{2\lambda}\right), \\ B_2&=\frac{1}{2}\left(U^3+V^2U+\frac{(K+4)U}{2\lambda}\right), \\ B_3&=\frac{1}{2}\left(V^3+U^2V+\frac{(K+4)V}{2\lambda}\right), \\ B_4&=\frac{1}{4}\left((U^2+V^2)^2+\frac{(K+4)(U^2+V^2)}{\lambda}+\frac{K^2+6K+8}{4\lambda^2}\right). \end{aligned}$$

Denoting

$$R_4=2b_4-\left(U^2+V^2+\frac{K+2}{2\lambda}\right)b_1, \quad R_3=b_3-Vb_1, \quad R_2=b_2-Ub_1,$$

the solution of Eq (A.5) can be expressed as

$$\begin{aligned} a_{x4}&=\frac{4\lambda^2}{K+2}(R_4-2UR_2-2VR_3), \\ a_{x3}&=2\lambda R_3-Va_{x4}, \quad a_{x2}=2\lambda R_2-Ua_{x4}, \\ a_{x1}&=b_1-Ua_{x2}-Va_{x3}-\frac{1}{2}a_{x4}\left(U^2+V^2+\frac{K+2}{2\lambda}\right). \end{aligned}$$

References

[1] Dinshaw S Balsara, Sudip Garain, and Chi-Wang Shu. An efficient class of WENO schemes with adaptive order. *Journal of Computational Physics*, 326:780–804, 2016.

[2] P. L. Bhatnagar, E. P. Gross, and M. K. Krook. A model for collision processes in gases. I. Small amplitude processes in charged and neutral one-component systems. *Phys. Rev.*, 94(3):511–525, 1954.

[3] Rafael Borges, Monique Carmona, Bruno Costa, and Wai Sun Don. An improved weighted essentially non-oscillatory scheme for hyperbolic conservation laws. *Journal of Computational Physics*, 227(6):3191–3211, 2008.

[4] Sydeny Chapman and T. G. Cowling. The Mathematical Theory of Non-Uniform Gases. An Account of the Kinetic Theory of Viscosity, Thermal Conduction and Diffusion in Gases. *Cambridge: University Press*, 1970.

[5] Stéphane Clain, Steven Diot, and Raphaël Loubère. A high-order finite volume method for systems of conservation laws—multi-dimensional optimal order detection (MOOD). *Journal of Computational Physics*, 230(10):4028–4050, 2011.

[6] Bernardo Cockburn and Chi-Wang Shu. TVB Runge-Kutta local projection discontinuous Galerkin finite element method for conservation laws. II. General framework. *Mathematics of Computation*, 52(186):411–435, 1989.

[7] Bernardo Cockburn and Chi-Wang Shu. The Runge–Kutta discontinuous Galerkin method for conservation laws V: Multidimensional systems. *Journal of Computational Physics*, 141(2):199–224, 1998.

[8] Virginie Daru and Christian Tenaud. Evaluation of TVD high resolution schemes for unsteady viscous shocked flows. *Computers & Fluids*, 30(1):89–113, 2000.

[9] Nico Fleischmann, Stefan Adami, and Nikolaus A Adams. Numerical symmetry-preserving techniques for low-dissipation shock-capturing schemes. *Computers & Fluids*, 189:94–107, 2019.

[10] Zhen Gao, Xiao Wen, and Wai Sun Don. Enhanced robustness of the hybrid compact-WENO finite difference scheme for hyperbolic conservation laws with multi-resolution analysis and Tukey's boxplot method. *Journal of Scientific Computing*, 73:736–752, 2017.

[11] Gottlieb, Sigal, Ketcheson, David, I., Higgs, Daniel, Grant, Zachary, and Nemeth. Explicit strong stability preserving multistep Runge-Kutta methods. *Mathematics of Computation*, 86(304):747–769, 2017.

[12] Ami Harten, Bjorn Engquist, Stanley Osher, and Sukumar R Chakravarthy. Uniformly high order accurate essentially non-oscillatory schemes, III. *Journal of Computational Physics*, 131(1):3–47, 1997.

[13] Chieh-Sen Huang, Todd Arbogast, and Chenyu Tian. Multidimensional WENO-AO reconstructions using a simplified smoothness indicator and applications to conservation laws. *Journal of Scientific Computing*, 97(1):8, 2023.

[14] Cong Huang and Li Li Chen. A simple smoothness indicator for the WENO scheme with adaptive order. *Journal of Computational Physics*, 352:498–515, 2018.

[15] Xing Ji. *High-order non-compact and compact gas-kinetic schemes*. Hong Kong University of Science and Technology (Hong Kong), 2019.

[16] Xing Ji, Wei Shyy, and Kun Xu. A gradient compression-based compact high-order gas-kinetic scheme on 3D hybrid unstructured meshes. *International Journal of Computational Fluid Dynamics*, 35(7):485–509, 2021.

[17] Xing Ji, Fengxiang Zhao, Wei Shyy, and Kun Xu. A HWENO reconstruction based high-order compact gas-kinetic scheme on unstructured mesh. *Journal of Computational Physics*, 410:109367, 2020.

[18] Xing Ji, Fengxiang Zhao, Wei Shyy, and Kun Xu. Compact high-order gas-kinetic scheme for three-dimensional flow simulations. *AIAA Journal*, (3):1–18, 2021.

[19] Guang-Shan Jiang and Chi-Wang Shu. Efficient implementation of weighted ENO schemes. *Journal of Computational Physics*, 126(1):202–228, 1996.

[20] Rakesh Kumar and Praveen Chandrashekar. Simple smoothness indicator and multi-level adaptive order WENO scheme for hyperbolic conservation laws. *Journal of Computational Physics*, 375:1059–1090, 2018.

[21] Rakesh Kumar and Praveen Chandrashekar. Efficient seventh order WENO schemes of

adaptive order for hyperbolic conservation laws. *Computers & Fluids*, 190:49–76, 2019.

[22] Peter D. Lax and Xu Dong Liu. Solution of two-dimensional Riemann problems of gas dynamics by positive schemes. *Siam Journal on Scientific Computing*, 19(2):319–340, 1998.

[23] Jiequan Li and Zhifang Du. A two-stage fourth order time-accurate discretization for Lax-Wendroff type flow solvers. I. Hyperbolic conservation laws. *SIAM Journal on Scientific Computing*, 38(5), 2015.

[24] Shiyi Li, Dongmi Luo, Jianxian Qiu, Song Jiang, and Yibing Chen. A one-stage high-order gas-kinetic scheme for multi-component flows with interface-sharpening technique. *Journal of Computational Physics*, 490:112318, 2023.

[25] Hongxu Liu and Xiangmin Jiao. WLS-ENO: Weighted-least-squares based essentially non-oscillatory schemes for finite volume methods on unstructured meshes. *Journal of Computational Physics*, 314:749–773, 2016.

[26] Xu-Dong Liu, Stanley Osher, and Tony Chan. Weighted essentially non-oscillatory schemes. *Journal of Computational Physics*, 115(1):200–212, 1994.

[27] Yuan Liu and Yong-Tao Zhang. A robust reconstruction for unstructured WENO schemes. *Journal of Scientific Computing*, 54:603–621, 2013.

[28] Liang Pan and Kun Xu. A third-order compact gas-kinetic scheme on unstructured meshes for compressible Navier–Stokes solutions. *Journal of Computational Physics*, 318:327–348, 2016.

[29] Liang Pan, Kun Xu, Qibing Li, and Jiequan Li. An efficient and accurate two-stage fourth-order gas-kinetic scheme for the Euler and Navier–Stokes equations. *Journal of Computational Physics*, 326:197–221, 2016.

[30] Chi-Wang Shu and Stanley Osher. Efficient implementation of essentially non-oscillatory shock-capturing schemes. *Journal of Computational Physics*, 77(2):439–471, 1988.

[31] E. F. Toro. *Riemann Solvers and Numerical Methods for Fluid Dynamics*. Springer Berlin Heidelberg, 2013.

[32] Geert Dick van Albada, Bram Van Leer, and WW Roberts Jr. A comparative study of computational methods in cosmic gas dynamics. *Astronomy and Astrophysics*, 108:76–84, 1982.

[33] P. Woodward and Phillip Colella. The numerical simulation of two-dimensional fluid flow with strong shocks. 1984.

[34] Kun Xu. Gas-kinetic schemes for unsteady compressible flow simulations. *Computational Fluid Dynamics, Annual Lecture Series, 29th, Rhode-Saint-Genese, Belgium*, 1998.

[35] Kun Xu. A gas-kinetic BGK scheme for the Navier–Stokes equations and its connection with artificial dissipation and Godunov method. *Journal of Computational Physics*, 171(1):289–335, 2001.

[36] C. W. Zhang. On positivity-preserving high order discontinuous Galerkin schemes for compressible Euler equations on rectangular meshes. *Journal of Computational Physics*, 229(23), 2010.

[37] Hong Zhang, Xing Ji, Yue Zhao, Yuan Ding, and Kun Xu. A robustness-enhanced reconstruction based on discontinuity feedback factor for high-order finite volume scheme. *Journal of Scientific Computing*, 101(1):20, 2024.